

# SAMUS: Adapting Segment Anything Model for Clinically-Friendly and Generalizable Ultrasound Image Segmentation

Xian Lin<sup>1</sup>, Yangyang Xiang<sup>1</sup>, Li Zhang<sup>2</sup>, Xin Yang<sup>1</sup>, Zengqiang Yan<sup>1\*</sup>, Li Yu<sup>1</sup>

<sup>1</sup>School of Electronic Information and Communications, Huazhong University of Science and Technology,  
<sup>2</sup>Union Hospital, Tongji Medical College, Huazhong University of Science and Technology

## Abstract

Segment anything model (SAM), an eminent universal image segmentation model, has recently gathered considerable attention within the domain of medical image segmentation. Despite the remarkable performance of SAM on natural images, it grapples with significant performance degradation and limited generalization when confronted with medical images, particularly with those involving objects of low contrast, faint boundaries, intricate shapes, and diminutive sizes. In this paper, we propose SAMUS, a universal model tailored for ultrasound image segmentation. In contrast to previous SAM-based universal models, SAMUS pursues not only better generalization but also lower deployment cost, rendering it more suitable for clinical applications. Specifically, based on SAM, a parallel CNN branch is introduced to inject local features into the ViT encoder through cross-branch attention for better medical image segmentation. Then, a position adapter and a feature adapter are developed to adapt SAM from natural to medical domains and from requiring large-size inputs ( $1024 \times 1024$ ) to small-size inputs ( $256 \times 256$ ) for more clinical-friendly deployment. A comprehensive ultrasound dataset, comprising about 30k images and 69k masks and covering six object categories, is collected for verification. Extensive comparison experiments demonstrate SAMUS's superiority against the state-of-the-art task-specific models and universal foundation models under both task-specific evaluation and generalization evaluation. Moreover, SAMUS is deployable on entry-level GPUs, as it has been liberated from the constraints of long sequence encoding. The code, data, and models will be released at <https://github.com/xianlin7/SAMUS>.

## 1 Introduction

Medical image segmentation, a crucial technology to discern and highlight specific organs, tissues, and lesions within medical images, serves as an integral component of computer-aided diagnosis systems (Liu et al. 2021). Numerous deep-learning models have been proposed for automatic medical image segmentation, showcasing substantial potential (Ronneberger, Fischer, and Brox 2015; Wu et al. 2022). However, these models are tailored for specific objects and necessitate retraining when applied to other objects, resulting in great inconvenience for clinical use.

Segment anything model (SAM), serving as a versatile foundation model for vision segmentation, has garnered

considerable acclaim owing to its remarkable segmentation capabilities across diverse objects and robust zero-shot generalization capacity (Kirillov et al. 2023). According to user prompts, including points, bounding boxes, and coarse masks, SAM is capable of segmenting the corresponding objects. Therefore, through simple prompting, SAM can be effortlessly adapted to various segmentation applications. This paradigm enables the integration of multiple individual medical image segmentation tasks into a unified framework (*i.e.*, a universal model), greatly facilitating clinical deployment (Huang et al. 2023).

Despite constructing the largest dataset to date (*i.e.*, SA-1B), SAM encounters a rapid performance degradation in the medical domain due to the scarcity of reliable clinical annotations (Huang et al. 2023). Some foundation models have been proposed to adapt SAM to medical image segmentation by tuning SAM on medical datasets (Ma and Wang 2023; Wu et al. 2023). However, the same as SAM, they perform a no-overlap  $16 \times$  tokenization on the input images before feature modeling, which destroys the local information crucial for identifying small targets and boundaries, making them struggle to segment clinical objects with complex/threadlike shapes, weak boundaries, small sizes, or low contrast. Besides, most of them require inputs with the size of  $1024 \times 1024$ , causing a substantial burden on GPU consumption due to the generated long input sequence.

In this paper, we present SAMUS to transfer the exceptional segmentation performance and strong generalization ability of SAM to the domain of medical image segmentation, while reducing computational complexity. SAMUS inherits the ViT image encoder, prompt encoder, and mask decoder of SAM, with tailored designs to the image encoder. First, we shorten the sequence length of the ViT-branch by reducing the input size to lower the computational complexity. Then, a feature adapter and a position adapter are developed to fine-tune the ViT image encoder from natural to medical domains. To complement local (*i.e.*, low-level) information in the ViT image encoder, we introduce a parallel CNN-branch image encoder, running alongside the ViT-branch and propose a cross-branch attention module to enable each patch in the ViT-branch to assimilate local information from the CNN-branch. Furthermore, we construct a large ultrasound dataset called US30K to comprehensively evaluate the efficacy of SAMUS. Experimental

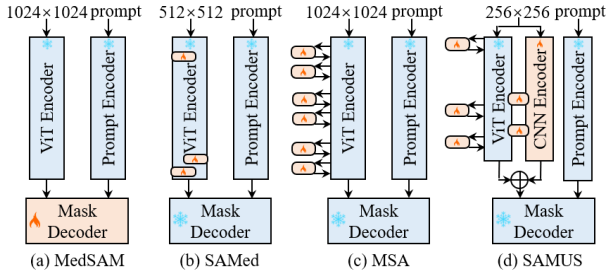


Figure 1: Structure comparison of different SAM-based foundation models for medical image segmentation.

results demonstrate that SAMUS outperforms the state-of-the-art methods in both task-specific and universal medical image segmentation. More importantly, SAMUS exhibits remarkable generalization capabilities, while considerably reducing the training cost compared to SAM. The contributions can be summarized as follows:

- A foundation model, SAMUS, designed for universal ultrasound image segmentation, requiring much fewer GPU resources compared to SAM.
- A CNN-branch image encoder and a cross-branch attention module to complement local information effectively to the ViT image encoder of SAM.
- A feature adapter and a position adapter to fine-tune the ViT-branch image encoder, further optimizing SAM for the medical domain
- A large ultrasonic dataset comprising 30,106 images with 68,570 masks to thoroughly evaluate the effectiveness of SAMUS.

## 2 Related Works

### 2.1 Visual Tuning

With the surprising development of foundation models in computer vision, a series of visual tuning approaches have been proposed to adapt these foundation models to downstream tasks. Generally, recent visual tuning approaches can be categorized into five main categories, including fine-tuning, parameter tuning, remapping tuning, prompt tuning, and adapt tuning (Yu et al. 2023). Specifically, fine-tuning methods involve either adjusting the entire parameter set of pre-trained models or selectively fine-tuning specific parts of pre-trained models (Ma and Wang 2023). Parameter tuning methods directly modify the weights or biases of model parameters (Lian et al. 2022). Remapping methods transfer the learned information from pre-trained models to downstream models through knowledge distillation, weight-based remapping, or architecture-based remapping (Zhao et al. 2022). Prompt tuning introduces the knowledge of downstream tasks by either incorporating a set of learnable parameters with the inputs or designing a sub-network to generate visual prompts (Wang et al. 2023). Adapter tuning, the most widely-adopted strategy, facilitates the learning of downstream tasks by incorporating additional learnable parameters with frozen pre-trained models (Wu et al. 2023).

### 2.2 Adapt SAM to Medical Image Segmentation

SAM has demonstrated remarkable performance in natural images but struggles with some medical image segmentation tasks, especially on objects with complex shapes, blurred boundaries, small sizes, or low contrast (Huang et al. 2023). To bridge this gap and enable SAM to adapt effectively to the medical image domain, several methods have been proposed to tune SAM using limited downstream medical datasets. MedSAM trains SAM on medical images at an acceptable cost by freezing the image encoder and the prompt encoder, focusing on tuning the mask decoder of SAM (Ma and Wang 2023). SAMed applies the low-rank-based (LoRA) strategy on the image encoder to tune SAM at a lower computational cost, making it more feasible for medical image segmentation (Zhang and Liu 2023). MSA adopts two down-ReLU-up adapters on each transformer layer of the ViT image encoder to introduce task-specific information (Wu et al. 2023). As illustrated in Fig. 1, compared to current SAM-based foundation models, the proposed SAMUS focuses more on complementing local features and reducing GPU consumption, which is crucial for accurate and easy-to-deploy medical image segmentation in clinical scenarios.

## 3 Methods

### 3.1 Overview

As depicted in Fig. 8, the overall architecture of SAMUS is inherited from SAM, retaining the structure and parameters of the prompt encoder and the mask decoder without any adjustment. Comparatively, the image encoder is carefully modified to address the challenges of inadequate local features and excessive computational memory consumption, making it more suitable for clinically-friendly segmentation. Major modifications include reducing the input size, overlapping the patch embedding, introducing adapters to the ViT branch, adding a CNN branch, and introducing cross-branch attention (CBA). Specifically, the input spatial resolution is scaled down from  $1024 \times 1024$  pixels to  $256 \times 256$  pixels, resulting in a substantial reduction in GPU memory cost due to the shorter input sequence in transformers. The overlapped patch embedding uses the same parameters as the patch embedding in SAM while its patch stride is half to the original stride, well keeping the information from patch boundaries. Adapters in the ViT branch include a position adapter and five feature adapters. The position adapter is to accommodate the global position embedding in shorter sequences due to the smaller input size. The first feature adapter follows the overlapped patch embedding to align input features with the required feature distribution of the pre-trained ViT image encoder. The remaining feature adapters are attached to the residual connections of the feed-forward network in the global transformer to fine-tune the pre-trained image encoder. In terms of the CNN branch, it is parallel to the ViT branch, providing complementary local information to the latter through the CBA module, which takes the ViT-branch features as the query and builds global dependency with features from the CNN branch. It should be noted that CBA is only integrated into each global transformer. Finally,

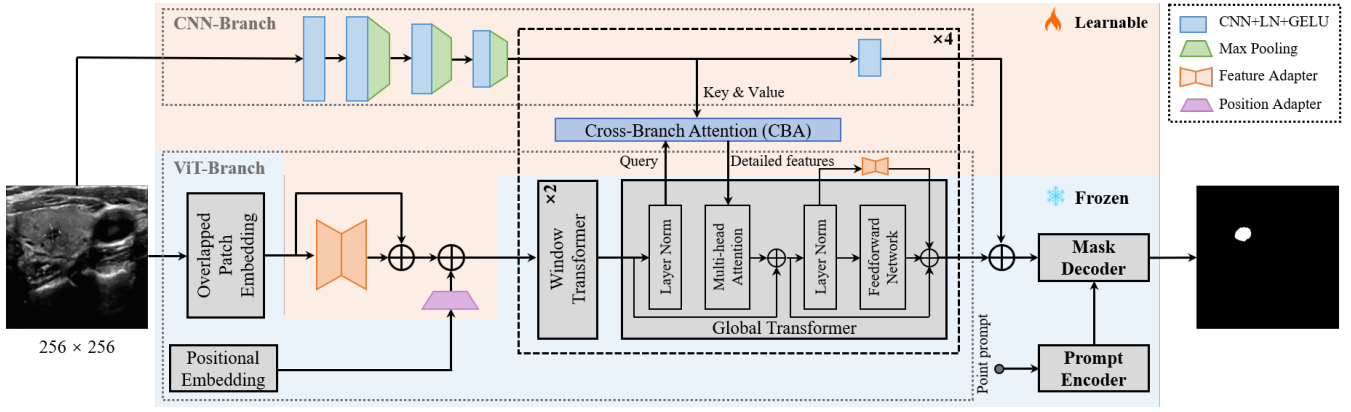


Figure 2: Overview of the proposed SAMUS.

the outputs of both the two branches are combined as the final image feature embedding of SAMUS.

### 3.2 Adapters in the ViT Branch

To facilitate the generalization of the trained image encoder (*i.e.*, the ViT branch) of SAM to smaller input sizes and the medical image domain, we introduce a position adapter and five feature adapters. These adapters can effectively tune the ViT branch while only requiring much fewer parameters. Specifically, the position adapter is responsible for adjusting the positional embedding to match the resolution of the embedded sequence. It begins by downsampling the positional embedding through a max pooling with the stride and kernel size as 2, achieving the same resolution as the embedded sequence. Subsequently, a convolution operation with a kernel size of  $3 \times 3$  is applied to tune the position embedding, further aiding the ViT branch in better handling smaller inputs. All feature adapters have the same structure that comprises three components: a down linear projection, an activation function, and an up linear projection. The procedure of each feature adapter can be formulated as:

$$\mathcal{A}(x) = \mathcal{G}(xE_d)E_u, \quad (1)$$

where  $\mathcal{G}$  represents the GELU activation function,  $E_d \in \mathbb{R}^{d \times \frac{d}{4}}$  and  $E_u \in \mathbb{R}^{\frac{d}{4} \times d}$  are the projection matrices,  $d$  is the dimension of the feature embedding. Through these simple operations, feature adapters enable the ViT branch to better adapt to the feature distribution of medical image domains.

### 3.3 The CNN Branch

The CNN branch consists of sequentially-connected convolution-pooling blocks. Specifically, the inputs pass through a single convolution block initially, followed by being processed through three convolution-pooling blocks. Then, the feature maps in the CNN branch share the same spatial resolution as those of the ViT branch. In the rest part of the CNN branch, such single convolution blocks are repeated four times in sequence. More details are illustrated in Fig. 8. This minimalist and lightweight design of the CNN branch is to prevent overfitting during training.

### 3.4 Cross-branch Attention

The cross-branch attention (CBA) module creates a bridge between the CNN branch and the ViT branch to further complement missing local features with the ViT branch. For a pair of feature maps from the ViT branch  $F_v$  and the CNN branch  $F_c$ , cross-branch attention in the single head can be formulated as:

$$\mathcal{F}(F_v, F_c) = (\mathcal{S}(\frac{F_v E_q (F_c E_k)^T}{\sqrt{d_m}}) + R)(F_c E_v), \quad (2)$$

where  $\mathcal{S}$  represents the Softmax function.  $E_q \in \mathbb{R}^{d \times d_m}$ ,  $E_k \in \mathbb{R}^{d \times d_m}$ , and  $E_v \in \mathbb{R}^{d \times d_m}$  are the learnable weight matrices used to project  $F_c$  and  $F_v$  to different feature subspaces.  $R \in \mathbb{R}^{hw \times hw}$  is the relative position embedding, and  $d_m$  is the dimension of CBA. The final output of CBA is the linear combination of  $g$  such single-head attention.

### 3.5 Training Strategies

Before training, SAMUS initializes the parameters that are inherited from SAM using the weights trained on SA-1B. The remaining parameters are initialized randomly. During the training process, only the parameters from adapters, the CNN branch, and the CBA module are updated, while other parameters are kept frozen. The training process is supervised using a combined loss function, comprising the dice loss and the binary cross-entropy loss. For ease of use, SAMUS only uses the simplest positive point prompt. We mimic the process of experts providing prompts by randomly sampling a point in the foreground area of the label. SAMUS is trained by the Adam optimizer with an initial learning rate of 0.0001 and a batch size of 8 for 200 epochs.

## 4 Experiments

### 4.1 Datasets

To comprehensively evaluate the effectiveness of SAMUS, we have constructed a large ultrasonic dataset named US30K as summarized in Table 6, containing data from seven publicly-available datasets, including TN3K (Gong et al. 2023), DDTI (Pedraza et al. 2015), TG3K (Wunderling et al. 2017), BUSI (Al-Dhabyani et al. 2020), UDIAT (Yap

Dataset	Slice number	Mask number	Train slice	Validation slice	Test slice	Segmentation target
TN3K	3493	3493	2303	576	614	Thyroid nodule
DDTI	637	637	-	-	637	Thyroid nodule
TG3K	3585	3585	3226	359	-	Thyroid gland
BUSI	647	647	454	64	129	Breast cancer
UDIAT	163	163	-	-	163	Breast cancer
CAMUS	19232	57696	15315	1949	1968	LV, MYO, LA
HMC-QU	2349	2349	-	-	2349	MYO
US30K	30106	68570	21298	2948	5860	Above 6 categories

Table 1: Summary of the datasets in US30K. LV, MYO, and LA are short for the left ventricle, myocardium, and left atrium.

Method	TN3K		BUSI		CAMUS-LV		CAMUS-MYO		CAMUS-LA	
	Dice	HD	Dice	HD	Dice	HD	Dice	HD	Dice	HD
U-Net	79.01	34.12	78.11	33.60	93.56	9.90	86.86	16.87	91.00	12.91
CPFNet	79.43	33.07	80.56	27.98	93.32	9.63	86.68	16.51	91.51	12.26
CA-Net	80.52	33.65	81.88	28.67	93.59	9.77	87.21	<b>16.24</b>	91.28	12.22
CE-Net	80.37	32.79	81.60	29.19	93.31	9.65	86.47	16.66	91.14	12.39
AAU-Net	82.28	30.53	80.81	28.96	93.32	9.97	86.98	16.49	91.35	12.12
SwinUnet	70.08	44.13	67.23	47.02	91.72	12.80	84.46	20.25	89.80	14.74
SETR	67.80	44.11	68.22	40.37	92.82	11.34	86.20	18.27	90.52	13.91
MISSFormer	79.42	32.85	78.43	33.10	93.25	9.94	86.57	16.50	91.18	11.82
TransUNet	81.44	30.98	82.22	27.54	93.54	9.60	87.20	16.36	91.37	12.10
TransFuse	78.50	32.44	73.52	34.95	93.30	10.07	86.77	17.25	90.68	12.46
FAT-Net	80.45	32.77	82.16	28.55	93.59	<b>9.20</b>	87.19	15.93	91.55	12.05
H2Former	82.48	30.58	81.48	27.84	93.44	9.79	87.31	16.60	90.98	11.92
SAMUS	<b>84.45</b>	<b>28.22</b>	<b>85.77</b>	<b>25.49</b>	<b>93.73</b>	9.79	<b>87.46</b>	16.74	<b>91.58</b>	<b>11.60</b>

Table 2: Quantitative comparison of our SAMUS and SOTA task-specific methods on segmenting thyroid nodule (TN3K), breast cancer (BUSI), left ventricle (CAMUS-LV), myocardium (CAMUS-MYO), and left atrium (CAMUS-LA). The performance is evaluated by the Dice score (%) and Hausdorff distance (HD). The best results are marked in bold.

et al. 2020), CAMUS (Leclerc et al. 2019), and HMC-QU (Kiranyaz et al. 2020). The data in TN3K and TG3K is partitioned into train, validation, and test sets following TRFE (Gong et al. 2023). BUSI is randomly split into 7:1:2 for training, validation, and testing, respectively. CAMUS is divided into a train set and a test set first according to the challenge (Leclerc et al. 2019). Then, we randomly select 10% patients from the train set to validate the model and the rest data as the final training data. To evaluate the generalization of different models, the other datasets in US30K are unseen during the training and validation process. To evaluate the segmentation performance and generalization ability of SAMUS against the state-of-the-art (SOTA) task-specific methods, several SOTA methods are implemented and trained on TN3K, BUSI, and CAMUS datasets individually for comparison. Furthermore, the comparison between SAMUS and other foundation models is conducted by training them on the entire US30K dataset and evaluating them on separate tasks.

## 4.2 Compare with SOTA Task-specific Methods

**Comparison methods:** Twelve SOTA task-specific approaches are selected for comparison, covering CNN-

based, transformer-based, and CNN-Transformer hybrid approaches. CNN-based methods include U-Net (Ronneberger, Fischer, and Brox 2015), CPFNet (Feng et al. 2020), CA-Net (Gu et al. 2020), CE-Net (Gu et al. 2019), and AAU-Net (Chen et al. 2022). Transformer-based methods include SwinUnet (Cao et al. 2022), SETR (Zheng et al. 2021), and MISSFormer (Huang et al. 2022). CNN-Transformer hybrid methods include TransUNet (Chen et al. 2021), TransFuse (Zhang, Liu, and Hu 2021), FAT-Net (Wu et al. 2022), and H2Former (He et al. 2023).

**Quantitative results:** Quantitative results of different task-specific approaches on TN3K, BUSI, CAMUS-LV, CAMUS-MYO, and CAMUS-LA are summarized in Table 7. Among these state-of-the-art approaches, H2Former achieves the best performance on TN3K and CAMUS-MYO, leading to the average Dice scores of 82.48% and 87.31% respectively. TransUnet, CA-Net, and FAT-Net achieve the best performance on BUSI, CAMUS-LV, and CAMUS-LA respectively, with the average Dice scores of 82.22%, 93.59%, and 91.55%. Comparatively, SAMUS consistently achieves better performance on all five tasks including TN3K, BUSI, CAMUS-LV, CAMUS-MYO, and CAMUS-LA with the average Dice scores of 84.45%,

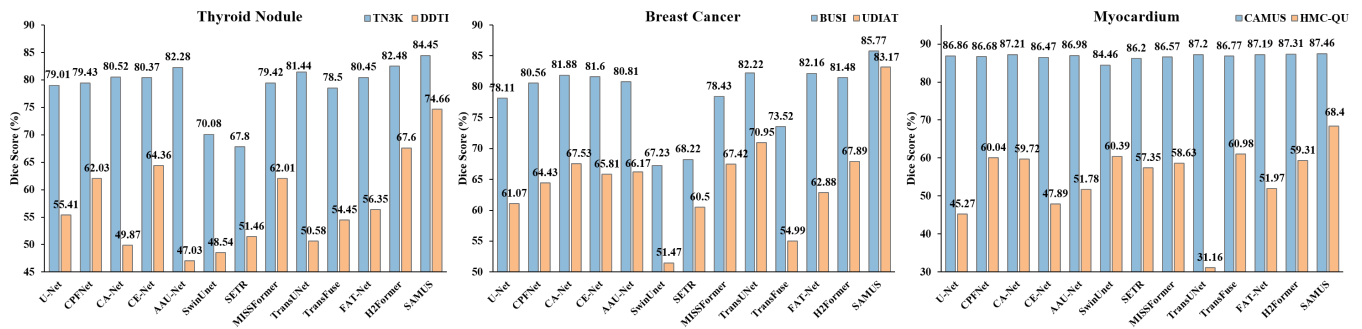


Figure 3: Comparison between SAMUS and task-specific methods evaluated on seeable (marked in blue) and unseen datasets (marked in orange).

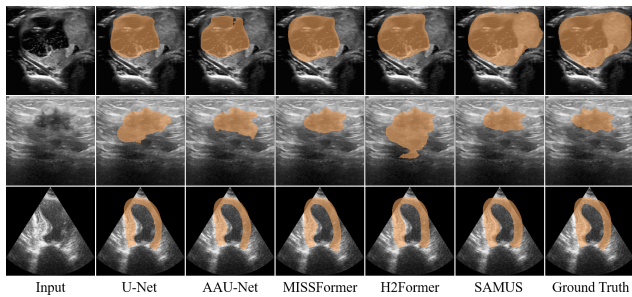


Figure 4: Qualitative comparisons between SAMUS and task-specific methods. From top to bottom are examples of segmenting thyroid nodule, breast cancer, and myocardium.

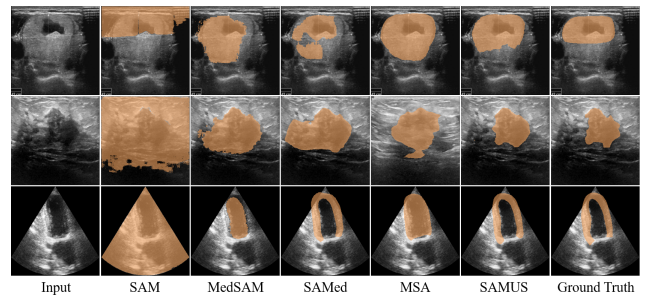


Figure 5: Qualitative comparisons between SAMUS and foundation models. From top to bottom are examples of segmenting thyroid nodule, breast cancer, and myocardium.

85.77%, 93.73%, 87.46%, and 91.58% respectively. It validates the effectiveness of adapting SAM to the medical image domain by SAMUS.

**Qualitative results:** Qualitative segmentation results of different methods, including U-Net (Ronneberger, Fischer, and Brox 2015), AAU-Net (Chen et al. 2022), MISSFormer (Huang et al. 2022), H2Former (He et al. 2023), and SAMUS, are illustrated in Fig. 4. Visually, segmenting the ultrasound images poses a challenge due to their low contrast, non-uniform features, and vague object boundaries. Existing methods struggle to accurately distinguish the target from the background, leading to extensive false negatives and/or false positives. Comparatively, SAMUS demonstrates superiority in preserving the integrity of target regions and reducing false positives. It is attributed to the inherent advantages of the SAM framework, as well as the specific adjustments and designs introduced in SAMUS.

**Generalization ability:** Quantitative comparison on the generalization performance of different task-specific methods is illustrated in Fig. 3. Among comparison methods, H2Former, TransUNet, and TransFuse achieve the best performance on DDTI, UDIAT, and HMC-QU respectively. Comparatively, SAMUS surpasses the best comparison method on each dataset with an average increase of 7.06%, 12.22%, and 7.42% in Dice respectively. Comparing the performance between seeable and unseen datasets, SAMUS encounters the least performance degradation in

contrast to other comparison methods across three different segmentation tasks. One interesting observation is that on the breast cancer segmentation task, the performance of SAMUS on the unseen dataset (*i.e.*, UDIAT) is even better than that of the best comparison method on the seeable dataset (*i.e.*, BUSI). It demonstrates the exceptional generalization ability of SAMUS in handling unseen domains, showcasing its robustness and adaptability across diverse medical image segmentation scenarios.

### 4.3 Compare with SOTA Foundation Models

**Comparison methods:** Four SOTA foundation models are selected for comparison, including the original SAM (Kirillov et al. 2023), MedSAM (Ma and Wang 2023), SAMed (Zhang and Liu 2023), and MSA (Wu et al. 2023).

**Quantitative results:** To validate the universal performance of SAMUS as a foundation model on diverse downstream tasks, we conduct a comparison among foundation models on the US30K dataset. As summarized in Table 8, SAM, the model trained on SA-1B, exhibits significant performance degradation on medical image segmentation without tuning. With simple fine-tuning on the mask decoder of SAM based on the US30K dataset, MedSAM considerably improves the performance of SAM. MAS, the best-performing model among comparison foundation models, effectively improves the segmentation performance of SAM with an average increase of 53.08%, 27.65%, 62.77%, 53.05%, and 74.52%

Method	TN3K		BUSI		CAMUS-LV		CAMUS-MYO		CAMUS-LA	
	Dice	HD	Dice	HD	Dice	HD	Dice	HD	Dice	HD
SAM	29.59	134.87	54.01	82.39	28.18	196.64	29.42	184.10	17.28	193.70
MedSAM	71.09	42.91	77.75	34.26	87.52	15.28	76.07	25.72	88.06	15.70
SAMed	80.40	31.29	74.82	34.60	87.67	13.24	82.60	19.48	90.92	12.60
MSA	82.67	29.15	81.66	28.87	90.95	<b>11.29</b>	82.47	19.28	91.80	<b>11.59</b>
SAMUS	<b>83.05</b>	<b>28.82</b>	<b>84.54</b>	<b>27.24</b>	<b>91.13</b>	11.76	<b>83.11</b>	<b>18.99</b>	<b>92.00</b>	12.08

Table 3: Quantitative comparison of our SAMUS and other foundation models on seeable US30K data. The performance is evaluated by the Dice score (%) and Hausdorff distance (HD).

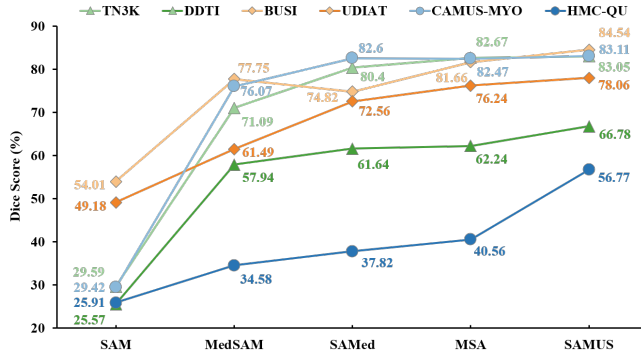


Figure 6: Segmentation and generalization ability comparison of our SAMUS and other foundation models on seeable (in light color) and unseen (in dark color) US30K data.

in Dice across TN3K, BUSI, CAMUS-LV, CAMUS-MYO, and CAMUS-LA. Compared to MSA, SAMUS consistently achieves remarkable improvements across the above five datasets, with superior Dice scores of 83.05%, 84.54%, 91.13%, 83.11%, and 92%, respectively. It validates the effectiveness of the CNN branch and the CBA module in SAMUS especially for complementing local information which is crucial for medical image segmentation.

**Qualitative results:** Qualitative segmentation results of different foundation models, including SAM, MedSAM, SAMed, MSA, and SAMUS, are presented in Fig. 5. Without tuning in medical images, SAM completely loses the ability to segment everything. Through applying tuning methods to SAM, MedSAM, SAMed, and MSA can somewhat restore the segmentation capability of SAM. However, they still struggle to accurately delineate segmentation boundaries in ultrasound images, resulting in extensive false negatives and false positives. In contrast, SAMUS exhibits superior performance by accurately locating segmentation boundaries, even for the low-contrast ones. It is consistent with the analysis that complementing local information with the image encoder is helpful, especially for boundary/shape preservation in medical image segmentation.

**Generalization ability:** Comparison of different foundation models on unseen domains is summarized in Fig. 6. In general, the generalization performance of foundation models trained on US30K in the medical image segmentation tasks is far better than that of the original SAM. In terms

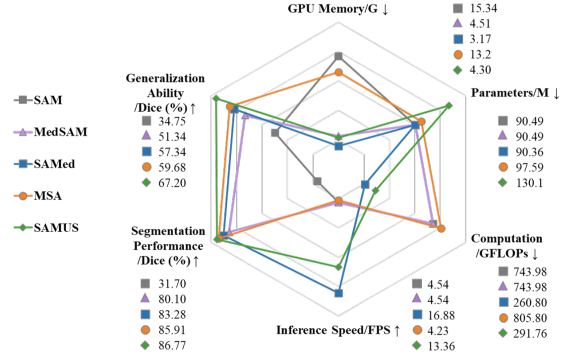


Figure 7: Comparison of SAMUS and foundation models on GPU memory cost, model parameters, computational complexity, inference speed, performance, and generalization.

of the three pairs of segmentation tasks, namely thyroid nodule segmentation, breast cancer segmentation, and myocardium segmentation, all foundation models encounter severe performance degradation on myocardium segmentation and generalize well on breast cancer segmentation. SAMUS consistently achieves the best performance across all three unseen datasets, leading to superior Dice scores of 66.78%, 78.06%, and 56.77% for the segmentation of thyroid nodule, breast cancer, and myocardium, respectively. It underscores the exceptional generalization ability of SAMUS, outperforming other foundation models consistently and substantially on unseen domains.

**Deployment cost:** We conducted a comprehensive evaluation of SAMUS and other foundation models on deployment efficiency, including GPU memory cost, model parameters, computational complexity, inference speed, segmentation performance, and generalization performance. For ease of comparison, the GPU memory is tested when batch size is set as 1 during training and measured by gigabyte (*i.e.*, G). The computational complexity and inference speed are measured by floating-point operations per second (*i.e.*, GFLOPs) and frame per second (*i.e.*, FPS). The segmentation performance is measured by the average Dice score across all seeable datasets and the generalization performance is evaluated based the average Dice score across all unseen datasets. All the above indicators are normalized and depicted with a radar plot as shown in Fig. 7. Among comparison models, SAMed exhibits the lowest GPU memory cost, model

CNN Branch	Components			TN3K		DDTI		BUSI		UDIAT	
	CBA	F-Adapter	P-Adapter	Dice	HD	Dice	HD	Dice	HD	Dice	HD
✗	✗	✗	✗	29.59	134.87	25.57	116.23	54.01	82.39	49.18	104.43
✓	✗	✗	✗	82.17	31.41	68.31	48.66	81.42	29.50	82.24	22.53
✓	✓	✗	✗	83.65	28.47	72.71	35.76	83.53	30.26	80.87	25.60
✗	✗	✓	✗	83.64	29.83	70.38	45.29	84.53	26.30	81.25	23.18
✗	✗	✗	✓	80.19	32.12	63.67	53.86	80.78	29.00	79.72	24.71
✓	✓	✓	✓	<b>84.45</b>	<b>28.22</b>	<b>74.66</b>	<b>21.03</b>	<b>85.77</b>	<b>25.49</b>	<b>83.17</b>	<b>21.25</b>

Table 4: Ablation study on different component combinations of SAMUS on the thyroid nodule and breast cancer segmentation. F-Adapter and P-Adapter represent the feature adapter and the position adapter respectively.

Prompt	TN3K		DDTI		BUSI		CAMUS-LV		CAMUS-MYO		CAMUS-LA	
	Dice	HD	Dice	HD	Dice	HD	Dice	HD	Dice	HD	Dice	HD
pt1	83.05	28.82	66.78	44.35	84.54	27.24	91.13	11.76	83.11	18.99	92.00	<b>12.08</b>
pt2	83.13	28.67	67.07	44.22	84.43	27.89	91.45	11.40	82.45	19.34	92.01	12.11
pt3	82.96	28.71	67.00	44.37	84.32	<b>26.96</b>	90.53	11.93	82.94	18.97	<b>92.03</b>	12.15
5 points	<b>83.98</b>	<b>28.24</b>	<b>68.93</b>	<b>43.87</b>	<b>85.20</b>	27.71	<b>92.95</b>	<b>10.60</b>	<b>87.20</b>	<b>17.19</b>	91.68	12.46
10 points	83.45	28.95	68.12	45.29	84.61	29.05	92.26	10.76	87.15	17.45	91.29	12.63

Table 5: Ablation study of different prompts. Pt1, pt2, and pt3 represent the single-point prompt in different (randomly determined) foreground positions. Multipoint prompts are generated by random sampling on the foreground areas.

parameters, computational complexity, and the fastest inference speed. However, its segmentation and generalization performance is inferior to both MSA and SAMUS. Though SAMUS owns more parameters than other models, its GPU memory cost and computational complexity are the second-fewest and its inference speed is the second-fastest, indicating that SAMUS is a more clinically-friendly model. Moreover, the deployment performance of SAMUS is quite close to that of the most easy-to-deploy method (*i.e.*, SAMed) with much better segmentation and generalization performance.

#### 4.4 Ablation Study

**Effectiveness of each component in SAMUS:** Four components in SAMUS, including the CNN branch, CBA, the feature adapter, and the position adapter, are introduced to the original SAM sequentially and trained on the TN3K and BUSI datasets for evaluation. As summarized in Table 9, coupling any component of SAMUS can effectively improve the segmentation performance and generalization ability of SAM on medical tasks. Even a simple position adapter can improve SAM by 50.6%, 38.1%, 26.77%, and 30.54% in Dice on TN3K, DDTI, BUSI, and UDIAT, respectively. By introducing local features, the CNN branch obtains more significant performance improvement than the position adapter. Besides, simply adding the outputs of the CNN branch and the ViT branch for fusion is not the best option. Introducing CBA can further promote the exploration of local features, thereby achieving an average increase of 1.48% and 2.11% in Dice compared to the CNN branch. By coupling all four components, SAMUS achieves the best segmentation performance and generalization.

**Effect of different prompts for SAMUS:** To analyze the

effect of prompts, we evaluate the performance of SAMUS trained on US30K under different point prompts. In general, SAMUS is robust to point locations and numbers. For objects with large within-class representation variations (*e.g.*, thyroid nodule, left ventricle, and myocardium), the segmentation performance varies within 1% in Dice under single-point prompts in different locations. Moreover, the performance can be improved greatly by introducing multipoint prompts. Comparatively, for objects with homogeneous features (*e.g.*, breast cancer and left atrium), performance variations under different single-point prompts are within the range of  $\pm 0.3\%$ , and introducing multipoint prompts would not necessarily bring performance gains. One possible reason is that using more points may produce information redundancy or exclusion.

## 5 Conclusion

In this paper, we propose SAMUS, a universal foundation model derived from SAM, for clinically-friendly and generalizable ultrasound image segmentation. Specifically, we present a parallel CNN branch image encoder, a feature adapter, a position adapter, and a cross-branch attention module to enrich the features for small-size objects and boundary areas while reducing GPU consumption. Furthermore, we construct a large ultrasound image dataset US30K, consisting of 30,106 images and 68,570 masks for evaluation and potential clinical usage. Experiments on both seeable and unseen domains demonstrate the outstanding segmentation ability and strong generalization ability of SAMUS. Moreover, the GPU memory cost of SAMUS is merely 28% of that required to train the entire SAM, and SAMUS is about  $3\times$  faster than SAM for inference.

## References

- Al-Dhabyani, W.; Gomaa, M.; Khaled, H.; and Fahmy, A. 2020. Dataset of breast ultrasound images. *Data in Brief*, 28: 104863.
- Cao, H.; Wang, Y.; Chen, J.; Jiang, D.; Zhang, X.; Tian, Q.; and Wang, M. 2022. Swin-unet: Unet-like pure transformer for medical image segmentation. In *European Conference on Computer Vision*, 205–218. Springer.
- Chen, G.; Li, L.; Dai, Y.; Zhang, J.; and Yap, M. H. 2022. AAU-net: an adaptive attention U-net for breast lesions segmentation in ultrasound images. *IEEE Transactions on Medical Imaging*.
- Chen, J.; Lu, Y.; Yu, Q.; Luo, X.; Adeli, E.; Wang, Y.; Lu, L.; Yuille, A. L.; and Zhou, Y. 2021. Transunet: Transformers make strong encoders for medical image segmentation. arXiv:2102.04306.
- Feng, S.; Zhao, H.; Shi, F.; Cheng, X.; Wang, M.; Ma, Y.; Xi-ang, D.; Zhu, W.; and Chen, X. 2020. CPFNet: Context pyramid fusion network for medical image segmentation. *IEEE Transactions on Medical Imaging*, 39(10): 3008–3018.
- Gong, H.; Chen, J.; Chen, G.; Li, H.; Li, G.; and Chen, F. 2023. Thyroid region prior guided attention for ultrasound segmentation of thyroid nodules. *Computers in Biology and Medicine*, 155: 106389.
- Gu, R.; Wang, G.; Song, T.; Huang, R.; Aertsen, M.; Deprest, J.; Ourselin, S.; Vercauteren, T.; and Zhang, S. 2020. CA-Net: Comprehensive attention convolutional neural networks for explainable medical image segmentation. *IEEE Transactions on Medical Imaging*, 40(2): 699–711.
- Gu, Z.; Cheng, J.; Fu, H.; Zhou, K.; Hao, H.; Zhao, Y.; Zhang, T.; Gao, S.; and Liu, J. 2019. Ce-net: Context encoder network for 2d medical image segmentation. *IEEE Transactions on Medical Imaging*, 38(10): 2281–2292.
- He, A.; Wang, K.; Li, T.; Du, C.; Xia, S.; and Fu, H. 2023. H2Former: An Efficient Hierarchical Hybrid Transformer for Medical Image Segmentation. *IEEE Transactions on Medical Imaging*.
- Huang, X.; Deng, Z.; Li, D.; Yuan, X.; and Fu, Y. 2022. Missformer: An effective transformer for 2d medical image segmentation. *IEEE Transactions on Medical Imaging*.
- Huang, Y.; Yang, X.; Liu, L.; Zhou, H.; Chang, A.; Zhou, X.; Chen, R.; Yu, J.; Chen, J.; Chen, C.; et al. 2023. Segment anything model for medical images? arXiv:2304.14660.
- Kiranyaz, S.; Degerli, A.; Hamid, T.; Mazhar, R.; Ahmed, R. E. F.; Abouhasera, R.; Zabihi, M.; Malik, J.; Hamila, R.; and Gabbouj, M. 2020. Left ventricular wall motion estimation by active polynomials for acute myocardial infarction detection. *IEEE Access*, 8: 210301–210317.
- Kirillov, A.; Mintun, E.; Ravi, N.; Mao, H.; Rolland, C.; Gustafson, L.; Xiao, T.; Whitehead, S.; Berg, A. C.; Lo, W.-Y.; et al. 2023. Segment anything. arXiv:2304.02643.
- Leclerc, S.; Smistad, E.; Pedrosa, J.; Østvik, A.; Cervenansky, F.; Espinosa, F.; Espeland, T.; Berg, E. A. R.; Jodoin, P.-M.; Grenier, T.; et al. 2019. Deep learning for segmentation using an open large-scale dataset in 2D echocardiography. *IEEE transactions on medical imaging*, 38(9): 2198–2210.
- Lian, D.; Zhou, D.; Feng, J.; and Wang, X. 2022. Scaling & shifting your features: A new baseline for efficient model tuning. In *Advances in Neural Information Processing Systems*, 109–123.
- Liu, X.; Song, L.; Liu, S.; and Zhang, Y. 2021. A review of deep-learning-based medical image segmentation methods. *Sustainability*, 13(3): 1224.
- Ma, J.; and Wang, B. 2023. Segment anything in medical images. arXiv:2304.12306.
- Pedraza, L.; Vargas, C.; Narváez, F.; Durán, O.; Muñoz, E.; and Romero, E. 2015. An open access thyroid ultrasound image database. In *10th International Symposium on Medical Information Processing and Analysis*, volume 9287, 188–193. SPIE.
- Ronneberger, O.; Fischer, P.; and Brox, T. 2015. U-net: Convolutional networks for biomedical image segmentation. In *International Conference on Medical Image Computing and Computer-Assisted Intervention*, 234–241. Springer.
- Wang, H.; Chang, J.; Luo, X.; Sun, J.; Lin, Z.; and Tian, Q. 2023. Lion: Implicit vision prompt tuning. arXiv:2303.09992.
- Wu, H.; Chen, S.; Chen, G.; Wang, W.; Lei, B.; and Wen, Z. 2022. FAT-Net: Feature adaptive transformers for automated skin lesion segmentation. *Medical Image Analysis*, 76: 102327.
- Wu, J.; Fu, R.; Fang, H.; Liu, Y.; Wang, Z.; Xu, Y.; Jin, Y.; and Arbel, T. 2023. Medical sam adapter: Adapting segment anything model for medical image segmentation. arXiv:2304.12620.
- Wunderling, T.; Golla, B.; Poudel, P.; Arens, C.; Friebe, M.; and Hansen, C. 2017. Comparison of thyroid segmentation techniques for 3D ultrasound. In *Medical Imaging*, volume 10133, 346–352. SPIE.
- Yap, M. H.; Goyal, M.; Osman, F.; Martí, R.; Denton, E.; Juette, A.; and Zwiggelhaar, R. 2020. Breast ultrasound region of interest detection and lesion localisation. *Artificial Intelligence in Medicine*, 107: 101880.
- Yu, B. X.; Chang, J.; Wang, H.; Liu, L.; Wang, S.; Wang, Z.; Lin, J.; Xie, L.; Li, H.; Lin, Z.; et al. 2023. Visual Tuning. arXiv:2305.06061.
- Zhang, K.; and Liu, D. 2023. Customized segment anything model for medical image segmentation. arXiv:2304.13785.
- Zhang, Y.; Liu, H.; and Hu, Q. 2021. Transfuse: Fusing transformers and cnns for medical image segmentation. In *International Conference on Medical Image Computing and Computer Assisted Intervention*, 14–24. Springer.
- Zhao, B.; Cui, Q.; Song, R.; Qiu, Y.; and Liang, J. 2022. Decoupled knowledge distillation. In *Proceedings of the IEEE/CVF Conference on computer vision and pattern recognition*, 11953–11962.
- Zheng, S.; Lu, J.; Zhao, H.; Zhu, X.; Luo, Z.; Wang, Y.; Fu, Y.; Feng, J.; Xiang, T.; Torr, P. H.; et al. 2021. Rethinking semantic segmentation from a sequence-to-sequence perspective with transformers. In *Proceedings of the IEEE/CVF Conference on Computer Vision and Pattern Recognition*, 6881–6890.



## A Appendix

### A.1 Details of Datasets

To comprehensively evaluate the effectiveness of SAMUS for ultrasound image segmentation, we construct a large ultrasonic dataset named US30K from publicly available datasets. The US30K covers 6 common categories in ultrasound images from seven datasets, containing 30106 images and 68570 masks in total. Details of each selected dataset are as follows:

(1) **TN3K**: a large thyroid nodule dataset includes 3493 ultrasound images with pixel-wise thyroid nodule annotations (Gong et al. 2023). The dataset was collected at Zhujiang Hospital, South Medical University from three different kinds of ultrasonic imaging devices, including RESONA 70B, ARIETTA 850, and GE Logiq E9. Following (Gong et al. 2023), the TN3K is split into 2303, 576, and 614 for training, validation, and testing. All images are pre-processed by (Gong et al. 2023).

(2) **DDTI**: a thyroid nodule dataset contains 637 ultrasound images with pixel-wise thyroid nodule annotations (Pedraza et al. 2015). DDTI was collected from two different kinds of ultrasonic imaging devices, including TOSHIBA Nemio 30 and TOSHIBA Nemio MX. We adopt the data pre-processed by (Gong et al. 2023). As the dataset has the same segmentation object with TN3K but with much fewer data, we treat this dataset as the unseen test set to evaluate the generalization ability of models.

(3) **TG3K**: a dataset originally designed to segment the thyroid gland region from the videos (Wunderling et al. 2017). (Gong et al. 2023) have pre-processed this dataset and constructed a new dataset covering 3585 images with pixel-wise thyroid gland annotations. Following (Gong et al. 2023), we adopt the pre-processed image dataset and split it into 3226 and 359 for training and validation.

(4) **BUSI**: a breast ultrasound dataset consists of 780 images with pixel-wise breast cancer annotations (Al-Dhabyani et al. 2020). BUSI was collected from two different kinds of ultrasonic imaging devices, including LOGIQ E9 and LOGIQ E9 Agile. Three classes of breast cases are concluded in BUSI, including 487, 210, and 133 for benign, malignant, and normal, respectively. All images are pre-processed by (Al-Dhabyani et al. 2020). As there is no publicly available data division, we randomly split BUSI into 7:1:2 for training, validation, and testing, respectively.

(5) **UDIAT**: a breast ultrasound dataset contains 163 images with pixel-wise breast cancer annotations (Yap et al. 2020). UDIAT was collected by Siemens ACUSON Sequoia C512 system. As the dataset has the same segmentation object as BUSI but with much fewer data, we treat this dataset as the unseen test set to evaluate the generalization ability of different models.

(6) **CAMUS**: a large fully annotated dataset for the purpose of 2D echocardiographic assessment (Leclerc et al. 2019). CAMUS was collected from GE Vivid E95 ultrasound scanners by the University Hospital of St Etienne. CAMUS consists of 500 patients and each patient contains a 2D apical four-chamber sequence and a two-chamber view sequence. Each sequence contains about 18 2D slices

and each slice contains the left ventricle (CAMUS-LV), myocardium (CAMUS-MYO), and left atrium (CAMUS-LA), three kinds of annotations. By splitting these 2D sequences into 2D images, we obtained 19232 images and 57696 masks in total. CAMUS is divided into a training-validation set and a test set first according to the challenge<sup>1</sup>. Then, we randomly split the training-validation set into 9:1 for training and validation.

(7) **HMC-QU**: a benchmark echo dataset collected by collaboration between Qatar University (QU) and Hamad Medical Corporation (HMC) Hospital in Doha, Qatar. HMC-QU contains publicly available 109 4-chamber sequences with pixel-wise myocardium annotations. By splitting these 2D sequences into 2D images, we obtained 2349 images. As the dataset has the same segmentation object as CAMUS-MYO but with much fewer data, we treat this dataset as the unseen test set to evaluate the generalization ability of models.

### A.2 Experiments

**Additional Implementation Details** All models were implemented within the PyTorch framework and trained on NVIDIA 3090ti GPUs and Intel(R) Xeon(R) Gold 6143 CPUs in the Linux operating system. When training SAMUS on task-specific datasets, we set the batch size equal to 8, one 3090ti GPU with memory of 24G is enough for training. When training SAMUS on US30K, the batch size is set as 32 to speed up the training. Four 3090ti GPUs are required for training. Names and versions of relevant software libraries would be released together with the code.

**Evaluation Metrics** To quantitatively evaluate the segmentation performance of the proposed SAMUS, we adopt the following six commonly used metrics (Chen et al. 2022; Gong et al. 2023):

- Dice (dice coefficient) =  $2TP/(FP+FN+2TP)$ .
- HD (haustofter distance) = the maximum distance between the predicted boundaries and ground truth.
- IoU (intersection over union) =  $TP/(FP+TP+FN)$ .
- ACC (accuracy) =  $(TN+TP)/(TN+TP+FN+FP)$ .
- SE (sensitivity) =  $TP/(TP+FN)$ .
- SP (specificity) =  $TN/(FP+TN)$ .

where TP, FP, TN, FN indicate true positive, false positive, true negative, and false negative, respectively.

**More Detailed Quantitative Results** Quantitative results on seeable datasets across six evaluation metrics are summarized in Tables 1-5. Generally, task-specific models can achieve a better performance than universal models on specific tasks. Training SAMUS on the task-specific dataset, SAMUS can achieve the best Dice and IoU across five tasks among task-specific models. Although the HD, ACC, SE, and SP of SAMUS are not optimal on individual datasets, they are the second-best or very close to the best performance. Quantitative results on unseen datasets are provided in Table 6-8. Among all models, SAMUS on specific-task datasets achieves the best Dice, HD, IoU, and ACC across

<sup>1</sup><https://www.creatis.insa-lyon.fr/Challenge/camus/>

Method	Dice/%	HD	IoU/%	ACC/%	SE/%	SP/%
U-Net	79.01±21.87	34.12±23.77	69.40±23.09	96.44±4.17	84.80±22.70	97.91±2.64
CPFNet	79.43±19.92	33.07±22.71	69.47±22.07	96.56±3.90	83.60±21.43	98.19±2.58
CA-Net	80.52±19.35	33.65±24.93	70.78±21.28	96.41±4.21	86.59±19.90	97.44±4.20
CE-Net	80.37±19.74	32.79±24.28	70.66±21.51	96.40±4.56	85.91±20.22	97.44±4.60
AAU-Net	82.28±18.86	30.53±23.07	73.16±20.80	96.88±4.23	85.68±19.85	<b>98.21±3.38</b>
SwinUnet	70.08±23.29	44.13±25.61	58.19±24.11	94.94±4.35	79.34±24.54	96.55±3.67
SETR	67.80±25.63	44.11±29.10	56.33±26.39	94.34±5.95	76.58±27.34	96.63±4.80
MISSFormer	79.42±21.43	32.85±25.03	69.86±22.92	96.37±4.32	84.39±22.68	97.64±3.86
TransUNet	81.44±19.31	30.98±21.68	72.05±21.08	96.94±3.26	87.13±20.38	97.75±3.08
TransFuse	78.50±21.60	32.44±23.17	68.60±22.86	96.44±3.96	82.06±23.69	97.95±3.11
FAT-Net	80.45±20.23	32.77±24.64	70.94±21.92	96.71±3.63	87.85±20.14	97.56±3.14
H2Former	82.48±18.30	30.58±22.10	73.31±20.41	96.95±3.59	85.30±19.34	98.09±3.25
SAMUS-TN3K	<b>84.45±15.00</b>	<b>28.22±19.71</b>	<b>75.33±17.60</b>	<b>97.21±3.41</b>	<b>88.38±15.60</b>	98.19±2.72
SAM	29.59±23.10	134.87±66.86	19.85±18.51	59.54±24.72	72.40±34.85	58.79±30.11
MedSAM	71.09±20.52	42.91±23.07	58.66±22.30	94.70±4.63	81.00±19.76	96.71±3.74
SAMed	80.40±19.51	31.29±21.82	70.62±21.29	96.68±3.49	86.74±20.15	97.75±2.95
MSA	82.67±16.58	29.15±20.80	73.08±18.89	96.85±3.84	89.38±17.22	97.91±2.71
SAMUS	<u>83.05±15.79</u>	<u>28.82±19.32</u>	<u>73.49±18.63</u>	<u>97.00±3.22</u>	<b>89.79±15.17</b>	97.71±3.00

Table 6: Quantitative comparison results on the seeable TN3K dataset. The top rows are the results of the task-specific models trained on TN3K, and the bottom rows are the results of the universal models trained on US30K. The best performance for each kind of model is underlined, and the best performance for all models is in bold.

Method	Dice/%	HD	IoU/%	ACC/%	SE/%	SP/%
U-Net	78.11±25.45	33.60±32.78	69.60±26.81	96.69±4.71	83.16±23.95	97.95±3.84
CPFNet	80.56±23.77	27.98±28.19	72.28±24.64	97.06±4.74	79.74±25.32	<b>98.83±2.36</b>
CA-Net	81.88±21.55	28.67±28.25	73.49±23.19	96.85±5.31	84.33±22.35	98.27±2.98
CE-Net	81.60±23.53	29.19±31.02	73.62±24.03	96.86±5.47	81.72±23.15	98.09±4.40
AAU-Net	80.81±23.55	28.96±30.06	72.69±25.14	96.76±5.71	82.77±23.96	98.36±4.70
SwinUnet	67.23±25.79	47.02±34.18	55.58±25.88	95.28±5.23	78.94±26.05	96.75±4.97
SETR	68.22±28.28	40.37±32.56	57.68±27.96	95.51±5.98	77.41±29.64	96.61±5.91
MISSFormer	78.43±24.99	33.10±35.08	69.73±25.76	96.26±5.96	83.24±24.08	97.55±5.17
TransUNet	82.22±24.08	27.54±28.25	74.77±24.57	97.26±4.84	83.19±25.18	98.69±3.82
TransFuse	73.52±28.16	34.95±37.18	64.28±28.05	96.21±5.85	78.61±28.57	97.69±5.34
FAT-Net	82.16±22.51	28.55±30.85	74.26±24.11	97.15±4.76	82.13±23.93	98.58±3.83
H2Former	81.48±22.91	27.84±27.02	73.34±24.13	96.68±5.50	85.16±22.93	97.71±5.17
SAMUS-BUSI	<b>85.77±16.53</b>	<b>25.49±28.10</b>	<b>77.79±18.93</b>	<b>97.47±4.88</b>	<b>87.65±16.48</b>	98.47±4.61
SAM	54.01±32.78	82.39±74.74	44.16±32.21	70.60±33.31	79.88±24.66	67.64±38.05
MedSAM	77.75±18.33	34.26±30.32	66.57±20.20	95.79±6.32	86.59±18.08	96.62±6.12
SAMed	74.82±26.88	34.60±37.66	65.37±26.45	95.97±6.67	82.62±28.97	97.47±5.32
MSA	81.66±19.25	28.87±28.42	72.42±21.35	96.92±5.03	<b>89.21±19.14</b>	97.69±4.76
SAMUS	<u>84.54±17.75</u>	<u>27.24±31.38</u>	<u>76.22±19.82</u>	<u>97.03±5.54</u>	88.35±17.11	<u>97.83±5.36</u>

Table 7: Quantitative comparison results on the seeable BUSI dataset. The top rows are the results of the task-specific models trained on BUSI, and the bottom rows are the results of the universal models trained on US30K. The best performance for each kind of model is underlined, and the best performance for all models is in bold.

three datasets. Generally, the generalization ability of universal models is better than that of the task-specific models on thyroid nodule segmentation and breast cancer segmentation. Among all the universal models, SAMUS shows the best Dice and IoU across three unseen datasets. It demonstrates the strong generalization ability of the proposed

SAMUS.

**Qualitative Results on Prompts** Qualitative results of different universal models on different prompts are provided in Fig. 8. The segmentation results of SAM and MedSAM under different prompts were notably different, while the

Method	Dice/%	HD	IoU/%	ACC/%	SE/%	SP/%
U-Net	93.56±2.43	9.90±4.30	88.00±4.18	98.84±0.70	93.85±3.42	99.36±0.65
CPFNet	93.32±2.37	9.63±3.85	87.57±4.08	98.82±0.62	93.73±3.78	99.36±0.47
CA-Net	93.59±2.13	9.77±3.60	88.02±3.65	98.87±0.58	93.73±3.13	<b>99.41±0.43</b>
CE-Net	93.31±2.46	9.65±3.65	87.55±4.24	98.81±0.66	94.19±3.45	99.31±0.58
AAU-Net	93.32±2.60	9.97±3.92	87.59±4.42	98.82±0.63	94.28±3.33	99.30±0.55
SwinUnet	91.72±2.69	12.80±4.47	84.82±4.45	98.55±0.73	91.34±4.18	99.32±0.58
SETR	92.82±3.10	11.34±4.60	86.76±5.14	98.75±0.65	93.62±4.07	99.28±0.62
MISSFormer	93.25±2.56	9.94±3.84	87.46±4.29	98.82±0.56	94.61±3.29	99.28±0.52
TransUNet	93.54±2.40	9.60±3.79	87.95±4.10	98.86±0.62	94.26±3.39	99.35±0.49
TransFuse	93.30±2.58	10.07±3.58	87.55±4.37	98.82±0.64	94.14±3.26	99.31±0.58
FAT-Net	93.59±2.33	<b>9.20±3.52</b>	88.04±4.02	98.86±0.59	<u>95.16±3.02</u>	99.26±0.57
H2Former	93.44±2.30	9.79±3.83	87.78±3.98	98.85±0.60	93.78±3.16	99.38±0.45
SAMUS-CAMUS-LV	<b>93.73±2.41</b>	9.79±3.67	<b>88.29±4.11</b>	<b>98.89±0.62</b>	94.58±3.07	99.35±0.47
SAM	28.18±8.76	196.64±12.68	16.73±6.36	56.30±3.63	<b>99.30±2.18</b>	52.22±2.65
MedSAM	87.52±5.64	15.28±4.95	78.22±8.27	97.68±1.44	92.66±5.71	98.26±0.98
SAMed	87.67±6.96	13.24±5.65	78.67±10.20	97.78±1.48	90.73±7.27	98.50±0.93
MSA	90.95±4.53	<u>11.29±4.70</u>	83.70±7.22	98.31±1.23	94.78±4.20	98.71±0.99
SAMUS	<u>91.13±4.72</u>	11.76±4.71	<u>84.03±7.57</u>	<u>98.34±1.33</u>	93.45±5.35	<u>98.88±0.77</u>

Table 8: Quantitative comparison results on the seeable CAMUS-LV dataset. The top rows are the results of the task-specific models trained on CAMUS-LV, and the bottom rows are the results of the universal models trained on US30K. The best performance for each kind of model is underlined, and the best performance for all models is in bold.

Method	Dice/%	HD	IoU/%	ACC/%	SE/%	SP/%
U-Net	86.86±3.83	16.87±5.99	76.97±5.82	97.27±1.54	87.11±5.88	98.53±0.86
CPFNet	86.68±3.73	16.51±5.58	76.68±5.70	97.27±1.44	86.70±5.37	98.54±0.84
CA-Net	87.21±3.38	16.24±4.80	77.48±5.19	<b>97.38±1.34</b>	87.34±4.83	98.56±0.88
CE-Net	86.47±4.02	16.66±5.76	76.38±6.11	97.23±1.49	86.03±5.72	98.58±0.85
AAU-Net	86.98±3.64	16.49±5.46	77.15±5.53	97.36±1.39	86.29±5.51	<b>98.66±0.82</b>
SwinUnet	84.46±4.00	20.25±6.53	73.30±5.80	96.76±1.64	86.80±5.63	98.00±0.96
SETR	86.20±4.66	18.27±6.77	76.03±6.84	97.15±1.58	86.80±5.43	98.38±1.11
MISSFormer	86.57±3.66	16.50±4.99	76.50±5.53	97.27±1.37	86.02±5.34	98.60±0.84
TransUNet	87.20±3.51	16.36±5.56	77.47±5.43	97.36±1.41	87.67±5.03	98.52±0.90
TransFuse	86.77±3.88	17.25±5.35	76.84±5.85	97.31±1.46	86.16±5.87	98.66±0.83
FAT-Net	87.19±3.51	<b>15.93±5.22</b>	77.45±5.37	97.38±1.40	87.06±5.27	98.62±0.81
H2Former	87.31±3.47	16.60±5.17	77.65±5.33	97.37±1.34	88.62±5.16	98.42±0.80
SAMUS-CAMUS-MYO	<b>87.46±3.50</b>	16.74±5.48	<b>77.88±5.38</b>	97.37±1.28	<u>89.98±4.26</u>	98.25±1.04
SAM	29.42±7.79	184.10±15.47	17.50±5.59	56.83±3.36	<b>92.25±9.46</b>	53.03±3.42
MedSAM	76.07±8.21	25.72±8.11	62.06±10.23	94.69±2.82	82.69±9.73	96.16±1.95
SAMed	82.60±6.07	19.48±5.95	70.80±8.56	96.42±1.83	84.22±7.09	97.84±1.21
MSA	82.47±5.99	19.28±6.11	70.60±8.36	96.30±1.96	85.34±7.29	97.63±1.24
SAMUS	<u>83.11±6.52</u>	<u>18.99±5.62</u>	<u>71.61±9.10</u>	<u>96.55±1.66</u>	85.29±6.92	<u>97.86±1.11</u>

Table 9: Quantitative comparison results on the seeable CAMUS-MYO dataset. The top rows are the results of the task-specific models trained on CAMUS-MYO, and the bottom rows are the results of the universal models trained on US30K. The best performance for each kind of model is underlined, and the best performance for all models is in bold.

segmentation results of SAMed, MSA, and SAMUS under different prompts were relatively similar. Furthermore, SAMUS can achieve better segmentation results based on a randomly sampled single-point prompt than that of other models under a multi-point prompt.

**Quantitative Results on Prompts** To analyze the effect of prompts, we evaluate the performance of SAMUS trained on US30K under different point prompts. In general, SAM and MedSAM are sensitive to the number and location of points, while SAMed, MSA, and SAMUS showed stable performance under different point prompts. Among all the univer-

Method	Dice/%	HD	IoU/%	ACC/%	SE/%	SP/%
U-Net	91.00±4.74	12.91±6.09	83.81±7.40	99.10±0.48	89.65±6.97	99.66±0.35
CPFNet	91.51±4.92	12.26±5.86	84.69±7.58	99.14±0.49	90.91±6.93	99.64±0.33
CA-Net	91.28±4.89	12.22±4.86	84.30±7.49	99.13±0.46	90.87±7.16	99.61±0.34
CE-Net	91.14±4.84	12.39±5.98	84.05±7.52	99.11±0.49	89.68±7.27	99.67±0.31
AAU-Net	91.35±4.13	12.12±5.47	84.33±6.55	99.14±0.43	89.79±6.55	99.69±0.31
SwinUnet	89.80±5.44	14.74±5.31	81.88±8.08	98.98±0.48	90.39±7.57	99.49±0.33
SETR	90.52±5.49	13.91±6.08	83.09±8.13	99.06±0.48	89.52±8.04	99.61±0.36
MISSFormer	91.18±4.76	11.82±4.74	84.11±7.41	99.11±0.49	90.75±6.89	99.61±0.37
TransUNet	91.37±4.49	12.10±5.46	84.41±7.14	99.13±0.47	90.15±6.86	99.66±0.37
TransFuse	90.68±4.84	12.46±5.40	83.28±7.47	99.08±0.49	88.44±7.82	99.70±0.28
FAT-Net	91.55±4.67	12.05±5.86	84.74±7.35	<u>99.15±0.46</u>	<u>91.02±6.82</u>	99.64±0.32
H2Former	90.98±4.72	11.92±5.57	83.76±7.36	99.12±0.46	88.31±7.38	<b>99.73±0.33</b>
SAMUS-CAMUS-LA	<u>91.58±4.26</u>	<u>11.60±4.33</u>	<u>84.74±6.74</u>	99.15±0.48	90.38±7.15	99.67±0.30
SAM	17.28±4.92	193.70±11.44	9.54±2.94	52.04±1.80	<b>94.84±9.72</b>	49.65±1.42
MedSAM	88.06±6.08	15.70±5.21	79.14±8.80	98.80±0.63	87.83±7.74	99.45±0.42
SAMed	90.92±4.90	12.60±5.27	83.69±7.56	99.09±0.46	90.85±6.76	<u>99.57±0.36</u>
MSA	91.80±4.49	<b>11.59±4.14</b>	85.13±7.09	99.16±0.44	92.61±6.19	99.55±0.37
SAMUS	<b>92.00±3.63</b>	12.08±4.58	<b>85.40±6.01</b>	<b>99.18±0.38</b>	93.58±4.45	99.50±0.39

Table 10: Quantitative comparison results on the seeable CAMUS-LA dataset. The top rows are the results of the task-specific models trained on CAMUS-LA, and the bottom rows are the results of the universal models trained on US30K. The best performance for each kind of model is underlined, and the best performance for all models is in bold..

Method	Dice/%	HD	IoU/%	ACC/%	SE/%	SP/%
U-Net	55.41±32.59	51.64±37.54	44.86±29.39	93.85±4.99	60.40±38.28	97.46±3.14
CPFNet	62.03±31.26	45.73±32.44	51.47±29.11	94.25±5.34	69.62±35.66	96.76±4.78
CA-Net	49.87±34.47	59.38±38.43	40.17±30.58	92.03±6.56	58.32±40.56	95.15±6.15
CE-Net	64.36±25.82	47.81±31.61	52.23±25.50	92.77±7.34	80.83±28.80	94.08±7.96
AAU-Net	47.03±38.83	54.38±39.98	39.43±34.51	94.13±5.21	49.84±43.09	<b>98.11±3.34</b>
SwinUnet	48.54±28.37	59.16±29.96	36.68±25.03	92.47±4.61	55.10±34.38	96.28±3.69
SETR	51.46±27.67	58.62±33.04	39.23±24.93	91.68±5.72	63.75±34.31	94.75±5.88
MISSFormer	62.01±32.06	43.57±31.82	51.82±30.04	94.41±5.37	68.95±36.33	96.70±5.15
TransUNet	50.58±36.96	54.97±38.74	41.94±33.00	93.91±5.30	56.79±43.00	97.39±3.84
TransFuse	54.45±34.05	54.29±39.45	44.58±31.00	93.20±6.10	60.84±39.22	96.75±4.32
FAT-Net	56.35±34.45	49.61±36.00	46.67±31.38	94.08±5.26	63.20±40.49	97.44±3.15
H2Former	67.60±27.45	43.96±33.48	56.51±26.71	94.33±5.31	79.06±30.08	95.92±5.25
SAMUS-TN3K	<b>74.66±21.03</b>	<b>36.09±26.24</b>	<b>63.35±22.82</b>	<b>95.15±4.85</b>	89.60±19.68	95.85±5.12
SAM	25.57±17.53	116.23±33.64	15.95±12.98	49.72±13.49	<b>97.70±13.92</b>	44.84±14.37
MedSAM	57.94±19.26	51.77±24.60	43.31±18.80	92.84±4.46	67.78±25.69	96.56±3.24
SAMed	61.64±31.11	<u>43.45±32.12</u>	50.97±28.93	<u>94.51±4.62</u>	71.03±36.61	<u>96.95±3.30</u>
MSA	62.24±30.27	46.49±34.69	51.36±28.55	93.81±5.20	73.93±34.75	95.94±3.67
SAMUS	<u>66.78±24.88</u>	44.35±30.07	<u>54.72±24.80</u>	93.45±5.94	85.57±25.43	94.23±6.45

Table 11: Quantitative comparison results on the unseen DDTI dataset. The top rows are the results of the task-specific models trained on TN3K, and the bottom rows are the results of the universal models trained on US30K. The best performance for each kind of model is underlined, and the best performance for all models is in bold.

sal models, SAMUS achieves the best segmentation performance across five evaluation metrics at any point prompt. It demonstrates that SAMUS is a powerful universal segmentation model that is robust to prompts.

Method	Dice/%	HD	IoU/%	ACC/%	SE/%	SP/%
U-Net	61.07±37.97	30.71±27.46	53.68±35.93	97.86±3.16	62.59±40.01	<b><u>99.26±1.50</u></b>
CPFNet	64.43±34.39	39.02±34.78	55.95±33.62	96.99±3.89	72.16±33.24	97.85±3.15
CA-Net	67.53±30.98	39.69±33.73	58.14±31.07	96.56±4.12	82.37±28.36	97.11±3.54
CE-Net	65.81±33.86	41.97±39.02	57.34±33.27	96.44±4.72	74.64±29.96	97.27±4.23
AAU-Net	66.17±31.19	42.67±35.74	56.71±31.64	96.34±4.42	83.97±27.04	96.91±3.82
SwinUnet	51.47±32.71	50.50±32.56	41.20±30.09	95.81±4.24	65.85±37.14	96.92±3.95
SETR	60.50±30.59	46.77±38.47	49.71±29.36	95.69±5.45	77.89±30.44	96.21±5.70
MISSFormer	67.42±31.59	41.06±41.31	58.33±31.76	96.11±5.53	80.28±25.67	96.73±5.21
TransUNet	70.95±33.01	26.38±23.40	63.09±32.05	98.04±3.00	73.93±34.59	98.96±1.51
TransFuse	54.99±35.43	47.25±39.29	45.87±32.92	95.59±5.85	70.06±37.55	96.23±5.94
FAT-Net	62.88±38.10	33.42±29.46	55.88±36.38	97.58±3.55	66.58±38.73	98.77±2.22
H2Former	67.89±31.88	40.94±41.43	59.00±31.91	96.28±4.89	81.58±28.99	96.74±4.64
SAMUS-BUSI	<b><u>83.17±16.69</u></b>	<b><u>21.25±21.26</u></b>	<b><u>73.90±19.20</u></b>	<b><u>98.40±2.83</u></b>	<b><u>91.59±11.03</u></b>	<b><u>98.73±2.21</u></b>
SAM	49.18±38.11	104.43±88.89	41.86±36.83	62.67±37.36	91.45±11.28	60.48±40.01
MedSAM	61.49±26.12	50.80±33.89	49.30±26.33	94.88±4.92	<b><u>96.19±10.95</u></b>	95.03±4.61
SAMed	72.56±25.54	30.82±33.12	61.98±25.42	97.14±4.71	87.43±23.79	97.71±3.70
MSA	76.24±23.08	<b><u>26.64±29.33</u></b>	65.96±23.72	97.38±4.60	90.87±19.31	<b><u>97.88±3.92</u></b>
SAMUS	<b><u>78.06±20.38</u></b>	26.91±29.97	<b><u>67.64±22.08</u></b>	<b><u>97.39±4.81</u></b>	92.18±15.33	97.70±4.39

Table 12: Quantitative comparison results on the unseen UDIAT dataset. The top rows are the results of the task-specific models trained on BUSI, and the bottom rows are the results of the universal models trained on US30K. The best performance for each kind of model is underlined, and the best performance for all models is in bold.

Method	Dice/%	HD	IoU/%	ACC/%	SE/%	SP/%
U-Net	45.27±19.07	26.25±6.67	31.17±15.62	96.23±0.99	44.26±24.35	98.48±1.18
CPFNet	60.04±13.05	24.12±6.12	44.12±13.17	96.32±1.16	69.54±18.05	97.42±1.17
CA-Net	59.72±14.95	23.94±6.99	44.13±14.72	96.29±1.28	69.05±18.02	97.43±1.14
CE-Net	47.89±14.55	28.49±6.33	32.69±12.73	95.47±1.12	55.00±23.27	97.16±1.35
AAU-Net	51.78±15.08	29.43±7.71	36.27±13.21	96.04±1.18	55.61±21.27	97.71±1.35
SwinUnet	60.39±10.89	28.26±7.70	44.11±11.00	95.63±1.46	79.84±10.72	96.30±1.47
SETR	57.35±9.65	27.75±7.15	40.86±9.69	95.51±1.38	72.85±10.51	96.47±1.31
MISSFormer	58.63±12.62	25.01±6.64	42.59±12.49	96.14±1.23	67.50±15.22	97.34±1.07
TransUNet	31.16±20.99	32.33±7.38	20.37±15.58	95.83±1.03	27.40±22.40	<b><u>98.77±0.88</u></b>
TransFuse	60.98±12.23	23.47±5.03	44.94±12.32	96.26±1.00	73.37±16.09	97.18±0.95
FAT-Net	51.97±13.79	28.22±6.37	36.27±12.53	95.83±1.09	58.24±20.53	97.43±1.13
H2Former	59.31±16.77	21.80±6.58	43.91±14.87	96.59±1.06	67.40±25.10	97.78±1.46
SAMUS-CAMUS-MYO	<b><u>68.40±10.61</u></b>	<b><u>20.61±7.09</u></b>	<b><u>52.93±11.90</u></b>	<b><u>96.88±1.26</u></b>	<b><u>82.13±13.96</u></b>	<b><u>97.50±1.34</u></b>
SAM	25.91±5.75	93.20±23.05	15.01±3.99	76.82±6.03	<b><u>95.74±13.91</u></b>	75.97±6.69
MedSAM	34.58±15.76	36.30±11.33	22.02±11.75	91.32±2.18	60.47±31.53	92.63±2.34
SAMed	37.82±16.57	37.72±10.05	24.67±13.31	91.14±3.47	62.43±22.70	92.37±3.18
MSA	40.56±16.93	38.18±13.39	26.87±13.57	91.45±3.19	70.27±27.22	92.32±3.19
SAMUS	<b><u>56.77±17.76</u></b>	<b><u>25.21±7.25</u></b>	<b><u>41.66±16.47</u></b>	<b><u>95.69±2.09</u></b>	68.89±22.19	<b><u>96.80±1.83</u></b>

Table 13: Quantitative comparison results on the unseen HMC-QU dataset. The top rows are the results of the task-specific models trained on CAMUS-MYO, and the bottom rows are the results of the universal models trained on US30K. The best performance for each kind of model is underlined, and the best performance for all models is in bold.

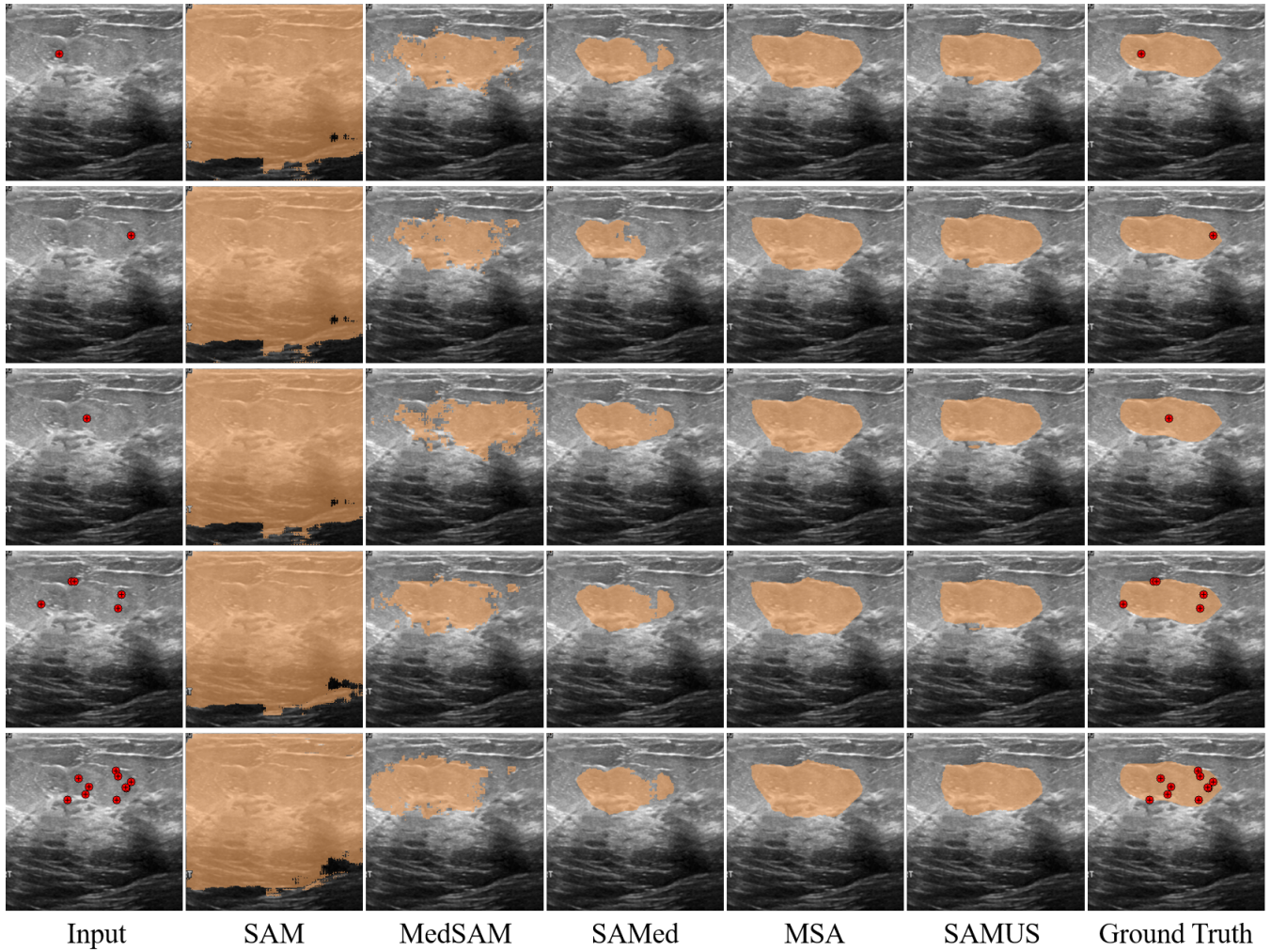


Figure 8: Qualitative comparison results on different prompts. The red circles with the cross indicate the location of the point prompt.

Method	Prompt	Dice/%	HD	IoU/%	ACC/%	SE/%	SP/%
SAM	pt1	54.01±32.78	82.40±74.75	44.16±32.21	70.60±33.31	79.88±24.66	67.64±38.06
	pt2	52.15±33.12	87.66±76.95	42.47±32.43	70.76±32.28	78.48±26.01	67.89±37.02
	pt3	54.02±33.31	82.05±74.43	44.36±32.51	72.55±32.41	77.26±27.66	70.20±37.49
	5 pts	60.02±30.26	82.05±75.04	49.42±30.59	76.58±27.97	84.65±15.15	73.77±32.17
	10 pts	63.99±28.98	75.44±71.05	53.31±29.70	79.54±26.15	86.19±10.60	76.92±30.39
MedSAM	pt1	77.75±18.33	34.26±30.34	66.57±20.21	95.79±6.32	86.59±18.08	96.62±6.12
	pt2	78.67±16.82	33.12±28.56	67.46±19.27	96.06±5.97	87.38±16.71	96.88±5.79
	pt3	77.83±17.97	34.04±28.50	66.60±20.01	96.10±5.02	86.32±18.42	96.98±4.86
	5 pts	76.90±17.99	34.91±25.93	65.37±20.16	96.01±4.88	90.28±16.22	96.39±5.19
	10 pts	76.23±17.11	36.91±27.04	64.29±19.87	95.70±5.04	92.41±13.11	95.79±5.85
SAMed	pt1	77.32±23.51	33.84±36.21	67.59±24.19	96.18±6.15	85.78±24.53	97.21±5.55
	pt2	77.63±23.08	33.37±35.38	67.85±23.80	96.27±6.04	85.63±24.30	97.33±5.40
	pt3	77.58±22.95	33.64±35.61	67.76±23.80	96.24±6.06	85.96±24.06	97.25±5.48
	5 pts	77.16±23.61	33.74±36.13	67.42±24.31	96.19±6.10	86.30±24.60	97.13±5.65
	10 pts	77.53±23.12	33.05±35.86	67.75±23.88	96.26±6.04	86.32±24.02	97.26±5.51
MSA	pt1	81.66±19.25	28.87±28.42	72.42±21.35	96.92±5.03	89.21±19.14	97.69±4.76
	pt2	81.57±19.60	28.96±28.75	72.37±21.46	96.95±4.93	89.06±20.04	97.75±4.60
	pt3	81.56±19.48	29.12±29.51	72.33±21.43	96.88±5.39	88.92±19.75	97.66±5.26
	5 pts	81.12±19.80	29.56±29.80	71.83±21.90	96.86±4.90	89.21±19.77	97.66±4.53
	10 pts	81.25±19.50	29.59±30.26	71.93±21.68	96.76±5.49	89.69±18.78	97.49±5.41
SAMUS	pt1	84.54±17.75	27.24±31.38	<b>76.22±19.82</b>	97.03±5.54	88.35±17.11	97.83±5.36
	pt2	84.43±17.59	27.89±31.67	76.03±19.86	96.97±5.64	88.45±16.38	97.78±5.40
	pt3	84.32±17.50	<b>26.96±29.66</b>	75.85±19.84	<b>97.09±5.33</b>	87.81±17.40	<b>97.98±4.96</b>
	5 pts	84.80±15.26	28.46±31.76	75.99±18.22	96.94±5.21	91.51±12.63	97.47±4.98
	10 pts	<b>84.98±14.86</b>	28.94±32.60	76.16±17.78	96.97±5.20	<b>93.13±11.03</b>	97.35±5.26

Table 14: Quantitative comparison results on different prompts. Pt1, pt2, and pt3 represent the single-point prompt in different (randomly determined) foreground positions. Multipoint prompts are generated by random sampling on the foreground areas.

## References

- Al-Dhabyani, W.; Gomaa, M.; Khaled, H.; and Fahmy, A. 2020. Dataset of breast ultrasound images. *Data in Brief*, 28: 104863.
- Cao, H.; Wang, Y.; Chen, J.; Jiang, D.; Zhang, X.; Tian, Q.; and Wang, M. 2022. Swin-unet: Unet-like pure transformer for medical image segmentation. In *European Conference on Computer Vision*, 205–218. Springer.
- Chen, G.; Li, L.; Dai, Y.; Zhang, J.; and Yap, M. H. 2022. AAU-net: an adaptive attention U-net for breast lesions segmentation in ultrasound images. *IEEE Transactions on Medical Imaging*.
- Chen, J.; Lu, Y.; Yu, Q.; Luo, X.; Adeli, E.; Wang, Y.; Lu, L.; Yuille, A. L.; and Zhou, Y. 2021. Transunet: Transformers make strong encoders for medical image segmentation. arXiv:2102.04306.
- Feng, S.; Zhao, H.; Shi, F.; Cheng, X.; Wang, M.; Ma, Y.; Xi-ang, D.; Zhu, W.; and Chen, X. 2020. CPFNet: Context pyramid fusion network for medical image segmentation. *IEEE Transactions on Medical Imaging*, 39(10): 3008–3018.
- Gong, H.; Chen, J.; Chen, G.; Li, H.; Li, G.; and Chen, F. 2023. Thyroid region prior guided attention for ultrasound segmentation of thyroid nodules. *Computers in Biology and Medicine*, 155: 106389.
- Gu, R.; Wang, G.; Song, T.; Huang, R.; Aertsen, M.; Deprest, J.; Ourselin, S.; Vercauteren, T.; and Zhang, S. 2020. CA-Net: Comprehensive attention convolutional neural networks for explainable medical image segmentation. *IEEE Transactions on Medical Imaging*, 40(2): 699–711.
- Gu, Z.; Cheng, J.; Fu, H.; Zhou, K.; Hao, H.; Zhao, Y.; Zhang, T.; Gao, S.; and Liu, J. 2019. Ce-net: Context encoder network for 2d medical image segmentation. *IEEE Transactions on Medical Imaging*, 38(10): 2281–2292.
- He, A.; Wang, K.; Li, T.; Du, C.; Xia, S.; and Fu, H. 2023. H2Former: An Efficient Hierarchical Hybrid Transformer for Medical Image Segmentation. *IEEE Transactions on Medical Imaging*.
- Huang, X.; Deng, Z.; Li, D.; Yuan, X.; and Fu, Y. 2022. Missformer: An effective transformer for 2d medical image segmentation. *IEEE Transactions on Medical Imaging*.
- Huang, Y.; Yang, X.; Liu, L.; Zhou, H.; Chang, A.; Zhou, X.; Chen, R.; Yu, J.; Chen, J.; Chen, C.; et al. 2023. Segment anything model for medical images? arXiv:2304.14660.
- Kiranyaz, S.; Degerli, A.; Hamid, T.; Mazhar, R.; Ahmed, R. E. F.; Abouhasera, R.; Zabihi, M.; Malik, J.; Hamila, R.; and Gabbouj, M. 2020. Left ventricular wall motion estimation by active polynomials for acute myocardial infarction detection. *IEEE Access*, 8: 210301–210317.
- Kirillov, A.; Mintun, E.; Ravi, N.; Mao, H.; Rolland, C.; Gustafson, L.; Xiao, T.; Whitehead, S.; Berg, A. C.; Lo, W.-Y.; et al. 2023. Segment anything. arXiv:2304.02643.
- Leclerc, S.; Smistad, E.; Pedrosa, J.; Østvik, A.; Cervenansky, F.; Espinosa, F.; Espeland, T.; Berg, E. A. R.; Jodoin, P.-M.; Grenier, T.; et al. 2019. Deep learning for segmentation using an open large-scale dataset in 2D echocardiography. *IEEE transactions on medical imaging*, 38(9): 2198–2210.
- Lian, D.; Zhou, D.; Feng, J.; and Wang, X. 2022. Scaling & shifting your features: A new baseline for efficient model tuning. In *Advances in Neural Information Processing Systems*, 109–123.
- Liu, X.; Song, L.; Liu, S.; and Zhang, Y. 2021. A review of deep-learning-based medical image segmentation methods. *Sustainability*, 13(3): 1224.
- Ma, J.; and Wang, B. 2023. Segment anything in medical images. arXiv:2304.12306.
- Pedraza, L.; Vargas, C.; Narváez, F.; Durán, O.; Muñoz, E.; and Romero, E. 2015. An open access thyroid ultrasound image database. In *10th International Symposium on Medical Information Processing and Analysis*, volume 9287, 188–193. SPIE.
- Ronneberger, O.; Fischer, P.; and Brox, T. 2015. U-net: Convolutional networks for biomedical image segmentation. In *International Conference on Medical Image Computing and Computer-Assisted Intervention*, 234–241. Springer.
- Wang, H.; Chang, J.; Luo, X.; Sun, J.; Lin, Z.; and Tian, Q. 2023. Lion: Implicit vision prompt tuning. arXiv:2303.09992.
- Wu, H.; Chen, S.; Chen, G.; Wang, W.; Lei, B.; and Wen, Z. 2022. FAT-Net: Feature adaptive transformers for automated skin lesion segmentation. *Medical Image Analysis*, 76: 102327.
- Wu, J.; Fu, R.; Fang, H.; Liu, Y.; Wang, Z.; Xu, Y.; Jin, Y.; and Arbel, T. 2023. Medical sam adapter: Adapting segment anything model for medical image segmentation. arXiv:2304.12620.
- Wunderling, T.; Golla, B.; Poudel, P.; Arens, C.; Friebe, M.; and Hansen, C. 2017. Comparison of thyroid segmentation techniques for 3D ultrasound. In *Medical Imaging*, volume 10133, 346–352. SPIE.
- Yap, M. H.; Goyal, M.; Osman, F.; Martí, R.; Denton, E.; Juette, A.; and Zwiggelaar, R. 2020. Breast ultrasound region of interest detection and lesion localisation. *Artificial Intelligence in Medicine*, 107: 101880.
- Yu, B. X.; Chang, J.; Wang, H.; Liu, L.; Wang, S.; Wang, Z.; Lin, J.; Xie, L.; Li, H.; Lin, Z.; et al. 2023. Visual Tuning. arXiv:2305.06061.
- Zhang, K.; and Liu, D. 2023. Customized segment anything model for medical image segmentation. arXiv:2304.13785.
- Zhang, Y.; Liu, H.; and Hu, Q. 2021. Transfuse: Fusing transformers and cnns for medical image segmentation. In *International Conference on Medical Image Computing and Computer Assisted Intervention*, 14–24. Springer.
- Zhao, B.; Cui, Q.; Song, R.; Qiu, Y.; and Liang, J. 2022. Decoupled knowledge distillation. In *Proceedings of the IEEE/CVF Conference on computer vision and pattern recognition*, 11953–11962.
- Zheng, S.; Lu, J.; Zhao, H.; Zhu, X.; Luo, Z.; Wang, Y.; Fu, Y.; Feng, J.; Xiang, T.; Torr, P. H.; et al. 2021. Rethinking semantic segmentation from a sequence-to-sequence perspective with transformers. In *Proceedings of the IEEE/CVF Conference on Computer Vision and Pattern Recognition*, 6881–6890.